ELSEVIER

Earth and Planetary Science Letters 186 (2001) 383–399

EPSL

www.elsevier.com/locate/epsl

Mantle compositional control on the extent of mantle melting, crust production, gravity anomaly, ridge morphology, and ridge segmentation: a case study at the Mid-Atlantic Ridge 33–35°N

Yaoling Niu [a,b,*], Daniel Bideau [c], Roger Hékinian [c], Rodey Batiza [d]

[a] *Department of Earth Sciences, Cardiff University, P.O. Box 914, Park Place, Cardiff CF10 3YE, UK*
[b] *ACQUIRE, The University of Queensland, Brisbane, Qld. 4072, Australia*
[c] *IFREMER, Centre de Brest, DRO/GM, B.P. 37, 29287 Plouzané, France*
[d] *National Science Foundation, Arlington, VA 22230, USA*

Received 3 March 2000; received in revised form 17 January 2001; accepted 24 January 2001

Abstract

Mantle temperature variation and plate spreading rate variation have been considered to be the two fundamental variables that determine the extent of mantle melting and ocean crust production. Along the length of a ~200 km portion of the Mid-Atlantic Ridge (MAR) between the Oceanographer (35°N) and Hayes (33°N) transforms, the mantle potential temperature is the same, the plate spreading rate is the same, but the extent of mantle melting and crustal production vary drastically. In addition to the typical crustal thickness variation on ridge segment scales at the MAR, i.e. thicker at segment centers and thinner at segment ends, there exist between-segment differences. For example, the ~90 km long segment OH-1 is magmatically robust with a central topographic high, thick crust, and a large negative gravity anomaly whereas the ~45 km long segment OH-3 is magmatically starved with a deep rift valley, thin crust and a weak negative gravity anomaly. We demonstrate that the observed differences in the extent of mantle melting, melt production and crustal mass between segments OH-1 and OH-3 are ultimately controlled by their fertile mantle source compositional difference as reflected by the lava compositional differences between the two segments: >70% of OH-1 samples studied ($N=57$) are enriched MORB with $[La/Sm]_N > 1$, but >85% of OH-3 samples studied ($N=42$) are depleted MORB with $[La/Sm]_N < 1$. Calculations show that the mean OH-1 source is more enriched in incompatible elements, total alkalis (~0.36 wt% Na_2O and ~0.09% K_2O) and H_2O content (~280 ppm) than the mean OH-3 source, which is depleted of incompatible elements, total alkalis (<0.17% Na_2O and <0.01% K_2O) and H_2O content (~70 ppm). These fertile compositional differences result in significantly reduced solidus temperature of OH-1 source over that of OH-3 source, and allows melting to begin at a significantly greater depth beneath OH-1 (~90 km) than beneath OH-3 (<60 km), leading to a taller melting column, higher degrees of decompression melting, greater melt production, thus thicker crust and more negative gravity anomaly at OH-1 than at OH-3. We emphasize that fertile mantle source compositional variation is as important as mantle temperature variation and plate spreading rate variation in governing the extent of mantle melting, crustal production, and MORB chemistry. The buoyancy-driven

* Corresponding author. Tel.: +44-29-2087-6411; Fax: +44-29-2087-4326; E-mail: niuy@cardiff.ac.uk

0012-821X/01/$ – see front matter
PII: S0012-821X(01)00255-2

focused mantle upwelling model better explains the observations than the subcrustal melt migration model. Future mantle flow models that consider the effect of fertile mantle compositional variation are expected to succeed in producing along-axis wavelengths of buoyant flow comparable to the observed size of ridge segments at the MAR. We propose that the size and fertility of the enriched mantle heterogeneities may actually control the initiation and evolution of ridge segments bounded by non-rigid discontinuities at slow-spreading ridges.

Keywords: Mid-Atlantic Ridge; mid-ocean ridge basalts; mantle; ridge segmentation; crust; ocean floor; gravity anomalies

1. Introduction

The ocean crust is the net product of magmatic, hydrothermal and tectonic processes operating within and below the global ocean ridge system. In contrast to the relative uniformity along the fast-spreading East Pacific Rise (EPR), crustal accretion at slow-spreading ridges, such as the Mid-Atlantic Ridge (MAR), is complex. The MAR is highly segmented to various lengths by both permanent transforms and non-rigid discontinuities, and has large variations in both across-axis morphology and along-axis topography [1,2]. Many MAR segments are characterized by a bathymetric high in the segment center, forming a three-dimensional (3-D) bathymetric structure on segment scales. Correlated with these bathymetric structures are circular gravity lows or 'bull's eyes' [3–5] interpreted to reflect an increase in crustal thickness from segment ends to the segment center by up to 4 km [3–7]. What is particularly important is the significant correlation of ridge segment length with the amplitude of the gravity anomaly and the magnitude of the inferred crustal thickness variation [3–5]. Long ridge segments are typically associated with large mantle Bouguer gravity lows, shallow hour-glass-shaped rift valleys that widen and deepen towards segment ends, and have greater mean crustal thickness and larger along-axis crustal variation. In contrast, short segments are characterized by smaller gravity lows, deeper and low-relief rift valleys, and have smaller along-axis crustal variation and thinner crust [3,5,8].

While these correlated variations are well-documented and point to a genetic link among these parameters, the nature of such a link remains unclear. The actual cause of the contrasting topography, morphology, gravity anomaly and crustal thickness between long and short ridge segments, particularly when they are in spatial proximity, is unknown. In this paper, we present geochemical data on densely sampled lavas from the two contrasting ridge segments (OH-1 and OH-3 in Fig. 1) between the Oceanographer and Hayes transforms along the MAR at 33–35°N. The data suggest that the fertile mantle compositional difference between OH-1 and OH-3 controls the observed differences between the two segments. Mantle source heterogeneity beneath ocean ridges is a well-known fact. Recent studies have in particular emphasized the mantle source (vs. processes) control on the observed MORB chemistry [9–12] and appealed to a discriminate use of MORB major element composition in estimating melting conditions [12,13]. However, the consequential role of fertile mantle compositional variation in determining the extent and depth of mantle melting and ocean crust production remains largely overlooked.

2. MAR at 33–35°N and samples

The MAR between the Hayes and Oceanographer transforms is one of the best-studied segments of the MAR. Reconnaissance studies along the North MAR by Schilling and co-workers [14,15] revealed the first-order physical and chemical consequences of plume–ridge interactions. The 1991 FARA-Sigma expedition [5,16] produced detailed bathymetric and gravity maps for the MAR extending from south of the Hayes transform at 33°N to the northern edge of the Azores Platform near 40°N. The 1992 FARA-Fazar expedition [17,18] allowed detailed sampling

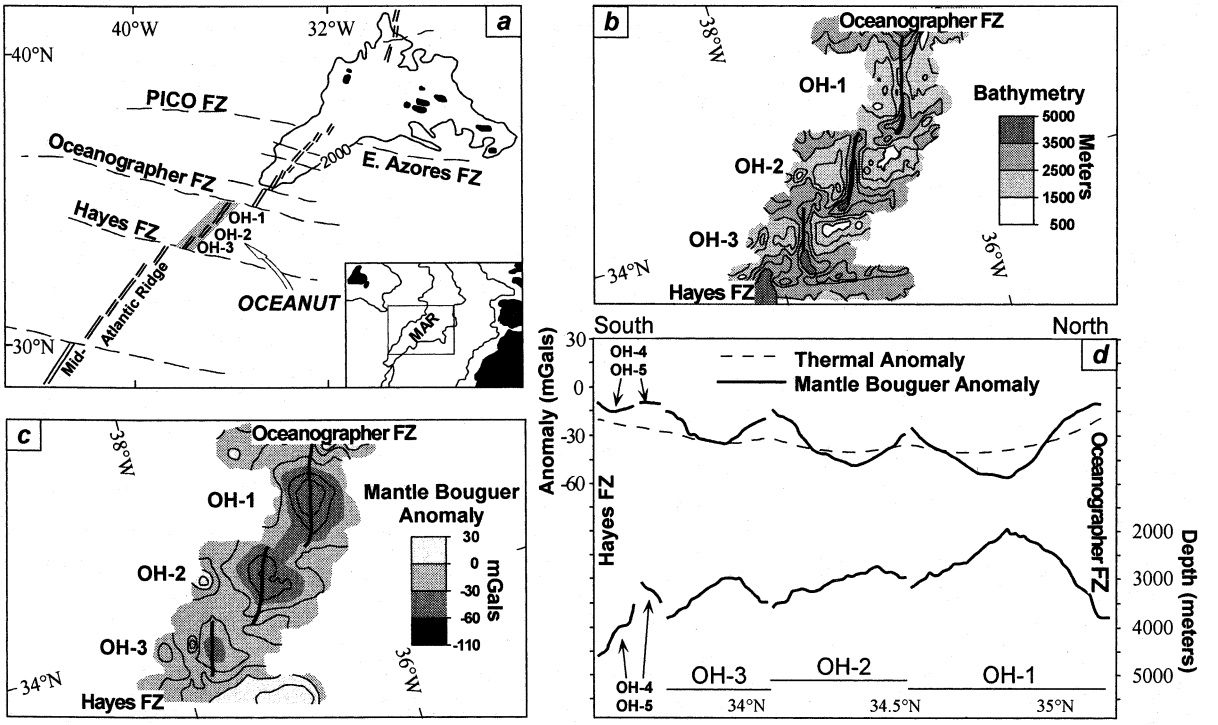

Fig. 1. a: Portion of the North MAR and the vicinity showing the study area between the Hayes and Oceanographer transforms during the *OCEANAUT* expedition after [19,20]. b and c: Simplified maps of the bathymetry and MBAs of the area. d: Along-axis profiles of ridge axial depth (bottom solid line), MBA (top solid line), and the interpreted thermal effect on the gravity anomalies. b, c and d are after [5].

along this same portion of the MAR. These early studies have targeted the Oceanographer–Hayes area for detailed investigations [7,8,19–26] because this area consists of contrasting ridge segments with distinctive topography, morphology and gravity anomalies, hinting at clues about crustal accretion processes at slow-spreading ridges.

The northern segment OH-1 is ~90 km long, and has a central topographic high with a median ridge (1700–2000 m), a chain of off-axis volcanoes trending at a high angle across the ridge axis, a large (~40 mGal peak-to-trough) negative mantle Bouguer anomaly (MBA), and a thick crust (Fig. 1). This segment is clearly magmatically robust [19–22] with possibly a magma chamber/lens present at its midpoint [23]. In contrast, segments OH-2 and OH-3 to the south are shorter (~59 and 45 km respectively), have deep (3000–3500 m) U-shaped axial valleys, and much smaller (~25 and <20 mGal respectively) MBAs. In situ submersible observations and exposures of mantle peridotites at the non-transform offset between OH-2 and OH-3 confirm the presence of anomalously thin crust due to starved magmatism [19–22] at these segments. The contrasting difference in melt generation and crust production on such a small (~200 km long Hayes–Oceanographer segment) geographic scale presents a challenge to our current theories. Mantle temperature variation [27–29] and plate spreading rate variation [13,30] are considered to be the primary controls on the extent of mantle melting and crustal production. As the plate spreading rate is essentially the same at these adjacent ridge segments, differences in mantle potential temperature would be invoked. Is the mantle hotter beneath OH-1 than beneath OH-2 and OH-3? Is it possible that the Azores hotspot to the north has greater thermal influence on OH-1 than on the more southerly OH-2 and OH-3? Is there any alternative mechanism that

may have led to the contrasting differences in mantle melting and crustal production? Geochemistry of basalts, the very product of mantle and crustal processes, must carry the message about the nature of these processes.

The 1995 *OCEANAUT* expedition aboard R/V *Nadir* with the submersible *Nautile* made significant in situ observations, and collected ~300 rock samples from magmatically robust OH-1 and starved OH-3 [19–22,26]. We discuss here the whole-rock major element data of 27 representative samples and whole-rock trace element data of 99 representative samples from the two ridge segments. Most samples studied are relatively fresh aphyric basalts. Some are fresh glasses, and others are plagioclase-phyric or plagioclase-olivine phyric basalts, for which only matrix portions were analyzed to avoid the effect of crystal accumulation. Some off-axis samples are apparently weathered, in which case mobile elements such as Rb, Cs, Pb, Li are apparently affected, and thus are not discussed.

3. Data and interpretations

Major elements on 13 OH-1 samples and 14 OH-3 samples were analyzed by ICP-AES at Université de Bretagne Occidentale [31]. Trace elements on 57 OH-1 samples and 42 OH-3 samples were analyzed by ICP-MS at the University of Queensland [32]. The complete analyses and sample descriptions are available on an **EPSL Online Background Dataset**[1]. Figs. 2–4 show the data graphically.

Fig. 2 shows variations of highly incompatible elements like Ba and Th and ratios of more-over-less incompatible elements such as Nb/Zr, $[La/Sm]_N$, $[Sm/Yb]_N$ and Zr/Y as a function of MgO and Na_2O for lavas from both OH-1 and OH-3. Lavas from OH-1 and OH-3 form distinctive groups. All but one OH-1 samples have lower MgO than OH-3 samples. OH-1 samples have on average significantly higher abundances and ratios of incompatible elements, including Na_2O than OH-3 samples. The low MgO and high Na_2O of the OH-1 samples could be interpreted solely as resulting from greater extents of frac-

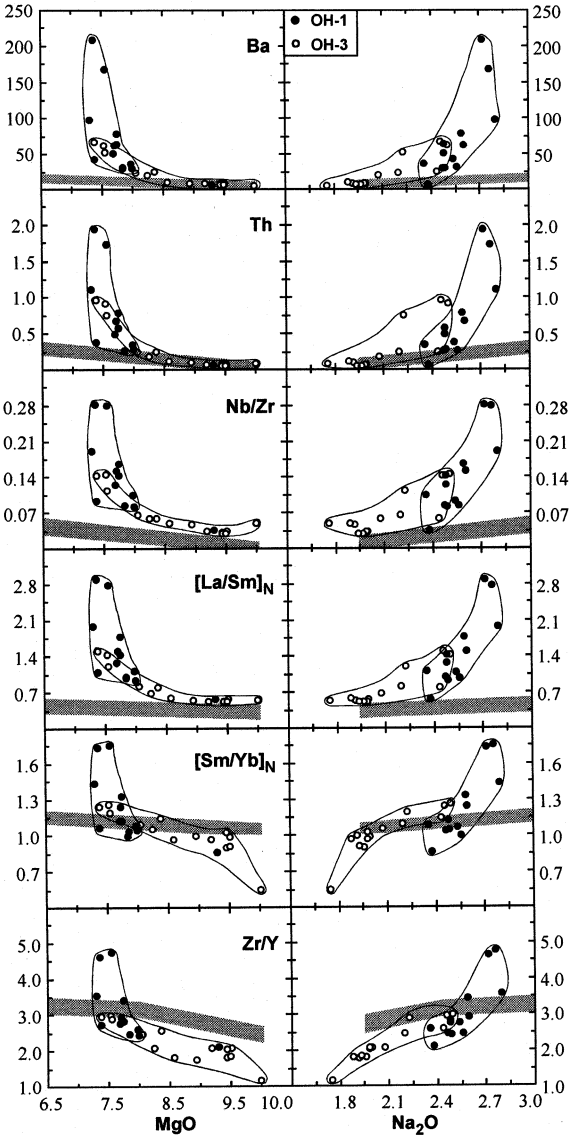

Fig. 2. Variations of incompatible element abundances (Ba and Th in ppm) and ratios (Nb/Zr, $[La/Sm]_N$, $[Sm/Yb]_N$ and Zr/Y; where the subscript N denotes chondrite-normalized values) as a function of MgO and Na_2O (wt%) for lavas from both ridge segments OH-1 and OH-3. The shaded bands indicate trends of low-pressure fractionation (with decreasing MgO and increasing Na_2O) on these plots derived form isotopically well-constrained N-type MORB from the northern EPR region [12,32,57].

[1] http://www.elsevier.nl/locate/epsl; mirror site: http://www.elsevier.com/locate/epsl

tionation than OH-3 samples, so could be the inverse correlations of MgO and positive correlations of Na_2O with the abundances and ratios of incompatible elements on these plots. However, neither the abundance levels nor detailed slopes defined by either OH-1 or OH-3 lavas can be explained by low-pressure fractionation as the latter would produce much shallower slopes as indicated by the shaded bands. High-pressure fractionation and the effect of varying volatile contents in primary melts would produce liquid lines of descent that differ from the low-pressure fractionation trends, but these would not cause significant fractionation in Nb/Zr, La/Sm, Sm/Yb and Zr/Y ratios. Therefore, the different abundance levels and incompatible element ratios defined by OH-1 and OH-3 lavas on these plots are not caused by fractionation, but inherited from their primary magmas.

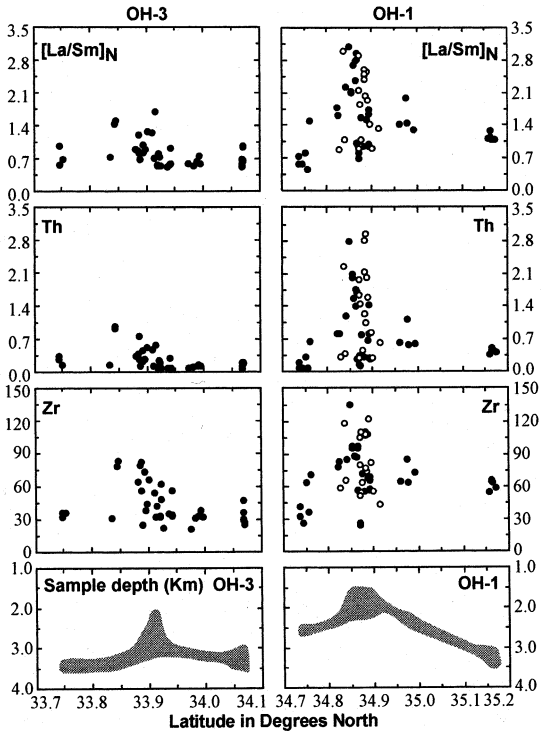

Fig. 3. Along-axis variation of Th and Zr abundances (ppm) and $[La/Sm]_N$ ratio to show that (1) large lava compositional variation exists on small scales at both OH-1 and OH-3; (2) highly depleted lavas with extremely low Th, Zr and $[La/Sm]_N$ exist at both OH-1 and OH-3, but lavas from OH-1 are on average significantly more enriched with many unusually enriched E-type MORB lavas ($[La/Sm]_N > 1.5$); and (3) less depleted or enriched lavas prefer to occupy the center of a segment in both cases with the maxima coinciding with the along-axis depth profile minima (bottom panels) and MBA maxima (Fig. 1b and d). Open symbols on OH-1 panels are off-axis samples. The shaded areas on the bottom panels are sampling depths.

If we assumed the abundances and ratios of these incompatible elements, including Na_2O, resulted from varying extents of melting only, then we cannot avoid the conclusion that OH-1 lavas were produced by very low extents of melting, whereas OH-3 lavas by very high extents of melting. This conclusion is undoubtedly wrong as it contradicts the observations! In fact, the large variation in incompatible element ratios in Fig. 2 can only be explained by melting compositionally heterogeneous sources [12–15,32,33].

Fig. 3 plots along-axis variation of $[La/Sm]_N$ and the abundances of representative incompatible elements like Th and Zr at OH-1 and OH-3. Highly depleted lavas with extremely low Th, Zr and $[La/Sm]_N$ exist at both OH-1 and OH-3, but lavas from OH-1 are on average significantly more enriched with many unusually enriched MORB lavas having $[La/Sm]_N > 1.5$ and up to 3.0, indicating the presence of an enriched and heterogeneous source beneath OH-1 (vs. OH-3). Note that the along-flowline off-axis samples (open circles) across central topographic high of OH-1 display a similar range to the axial lavas, suggesting that the large compositional range and 'spike' in the segment center defined by 'zero-age' lavas have been persistent in the last $\geq$2.5 Ma. Also note that less depleted or enriched lavas preferentially occupy the center of a segment at both OH-1 and OH-3 with the maxima coinciding with the along-axis depth profile minima (bottom panels) and MBA maxima (Fig. 1b and d). This phenomenon has been observed elsewhere along the MAR [17,18,33].

Plots of incompatible element abundances (e.g. Ba, U, Ta and Sr) and ratios of more-over-less incompatible elements (e.g. Nb/La, La/Sm, Zr/Y and Hf/Yb) as a function of axial depth reveal scattered yet significant correlations (Fig. 4). Depleted lavas dominate at deep portions of the ridge at both OH-1 and OH-3, but the highly

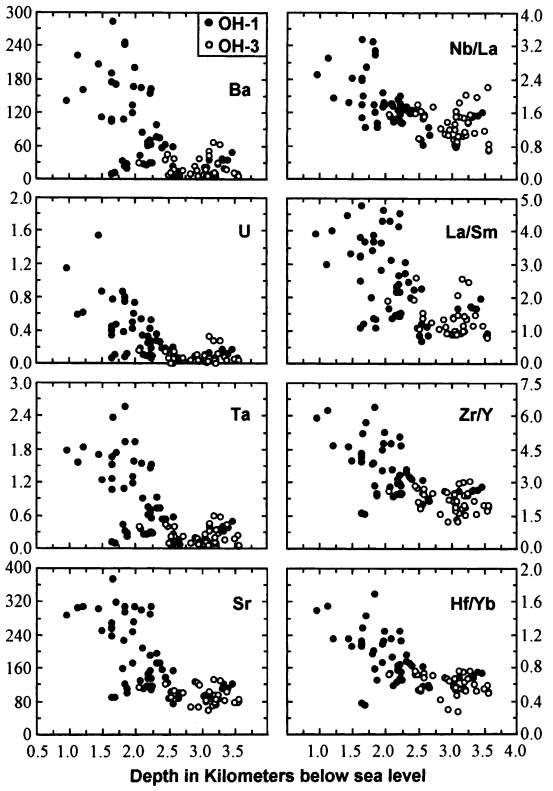

Fig. 4. Variations of representative incompatible element abundances (Ba, U, Ta and Sr in ppm) and ratios (Nb/La, La/Sm, Zr/Y and Hf/Yb) as a function of sampling depth for lavas from both OH-1 and OH-3.

enriched ones are exclusively associated with topographic high at OH-1. This observation reflects a genetic link between the topographic high and the enriched lavas that make up the high. Histograms (not shown) indicate that more than 70% OH-1 samples have $[La/Sm]_N > 1$ whereas more than 85% OH-3 samples have $[La/Sm]_N < 1$ (see **EPSL Online Background Dataset**[1]).

4. Discussion

The data and foregoing discussion raise two first-order questions: (1) Why are highly enriched lavas exclusive to magmatically robust OH-1, but absent at magmatically starved OH-3? (2) Why do enriched or less depleted lavas preferentially occupy the segment center? The questions can be answered by analyzing the contrasting differences between OH-1 and OH-3 in terms of fundamental variables that govern the magmatic accretion at ocean ridges.

4.1. The cause of the contrasting differences between OH-1 and OH-3

The inflated topography and morphology and large MBA at OH-1 (Fig. 1) and submersible observations indicate unequivocally that this segment is magmatically robust with a large crustal mass relative to OH-3, which is magmatically starved with a small crustal mass. Greater crustal mass results from a greater amount of mantle melt produced and extracted. Assuming complete melt extraction, then the crustal mass (M_c) produced per unit time is the product of the extent of melting (F) from a given parcel of fertile mantle and the amount of the fertile mantle melted (M_f) per unit time. That is, $M_c = F \times M_f$. As mantle melting beneath ridges results from decompression, M_f would be a function of mantle upwelling rate, which is in turn determined by (1) plate spreading rate (R) if sub-ridge mantle upwelling is mostly passive and (2) the component of dynamic upwelling. The dynamic upwelling is shown to increase with decreasing spreading rate [34], and must also depend on thermal (T) or compositional (X) buoyancy of the upwelling mantle relative to its surroundings. Therefore, $M_f = f(R,T,X)$. The extent of mantle melting beneath ocean ridges is generally thought to be controlled by mantle temperature variation [27–29] and plate spreading rate variation [13,30], but it must also depend on the composition of the fertile mantle material. More melt would form at a given mantle temperature and for a given amount of decompression from a mantle that contains more enriched component than a more refractory mantle. Thus, $F = f(R,T,X)$ is also true. Therefore, variations in plate spreading rate, mantle temperature and fertile mantle composition are the fundamental variables that determine the ultimate melt production and crustal mass at ocean ridges: $M_c = f(R,T,X)$.

As the plate spreading rate is essentially the same, $\sim$22 mm/yr [35] at both OH-1 and OH-3,

the effect of spreading rate variation can be ruled out as an influential factor, which leaves mantle temperature and source compositional differences as the possible controls. That is, $M_c = f(T,X)$.

4.1.1. Is the mantle beneath OH-1 necessarily hotter than the mantle beneath OH-3?

OH-1 lavas are highly enriched in incompatible elements including heat-producing K, U and Th relative to OH-3 lavas. Thus OH-1 mantle source region could be intrinsically hotter than OH-3 mantle source region. This effect certainly exists, but it must be insignificant because of the very long half-lives, thus very slow heat production, of these heat-producing isotopes compared to the essentially 'zero-age' process beneath ocean ridges. Furthermore, heat conduction is efficient, and thus it is difficult to generate and maintain a large thermal gradient at the mantle solidus depth on spatial scales as short as a few tens of kilometers such as between OH-1 and OH-3.

Detrick et al. [5] argued that the systematic southward deepening of the MAR rift valley and decrease in MBA between the Oceanographer and Hayes transforms are consequences of two effects. One is increasing distance from the Azores hotspot to the north, and the other is 'a systematic decrease in the segment length/offset ratio from north to south between the two transforms' ([5], p. 3775). These interpretations are inconsistent with the observations. If thermal influence of the Azores hotspot indeed caused the contrasting differences between OH-1 and OH-3, then ridge segments north of the Oceanographer transform (e.g. PO-8, PO-7) would have much greater effect. That is, these segments would have shallower axial depth, greater negative MBA, and more Azores-like basal compositions, but none of these is observed [5,17,18]. Fig. 5 shows that OH-1 has the greatest negative MBA of all the ridge segments studied at the North MAR, greater than all ridge segments closer to the Azores [3–5,24,25]. It is simply unlikely that the Azores hotspot would have greater thermal influence on OH-1 than on ridges closer to the hotspot itself. Therefore, the contrast between OH-1 and OH-3 cannot be ascribed to Azores' thermal effect.

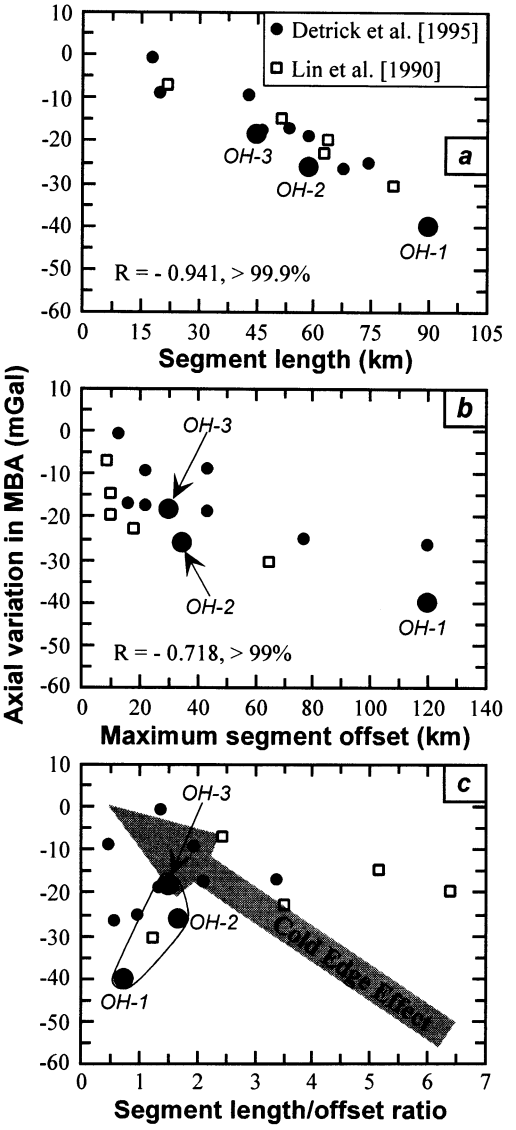

Fig. 5. Plots of axial variation in MBA (mGal) against (a) ridge segment length, (b) offset size and (c) length/offset ratio after [5]. Note that the well-defined significant inverse correlation in (a) and the scattered correlation in (b) point to an intrinsic link between these parameters in their origin. Note also that the non-correlation in (c) suggests that the origin of MBA is independent of 'cold-edge' effects at lithospheric levels, and thus must ultimately result from sublithospheric mantle processes. Open squares are data from the MAR 28–31°N [3] and solid circles are data from the MAR 33–37.5°N including OH-1, OH-2 and OH-3 [5]. The shaded arrow in (c) points to the direction of increasing 'cold-edge' effects.

Hence, the mantle source region is not hotter beneath OH-1 than beneath OH-3. It is possible that the enriched OH-1 material could have come from the Azores plume (i.e. a compositional effect), but this hypothesis is unsupported isotopically [18].

By using a passive, plate-driven mantle flow model, Detrick et al. [5] concluded that the mantle is hotter beneath OH-1 than beneath OH-2 and OH-3 by assuming a southward decrease in the segment length/offset ratio from north to south. This along-axis temperature variation would contribute to the observed MBA (the dashed line in Fig. 1d). Fig. 5c shows however that the segment length/offset ratio of OH-1 is the smallest, not highest. This means that if 'cold-edge' effect were important, OH-1 would be cooled most not only because of its low length/offset ratio, but also because of the cold and old (~10 Ma) lithosphere across the permanent Oceanographer transform to the north. In contrast, OH-2 and OH-3 are only offset by short non-permanent discontinuities, which are probably not even cold edges. The scatter in Fig. 5c demonstrates that along-ridge morphology, topography and MBA are independent of segment length/offset ratio, and thus are independent of the 'cold-edge' effect.

4.1.2. *Fertile mantle compositional control on the extent of mantle melting and crust production*

The above discussion leaves fertile mantle composition as the sole likely variable responsible for the contrasting differences between magmatically robust OH-1 and starved OH-3, i.e. $M_c = f(X)$. Indeed, the huge lava compositional differences between OH-1 and OH-3 (Figs. 2–4) can only be

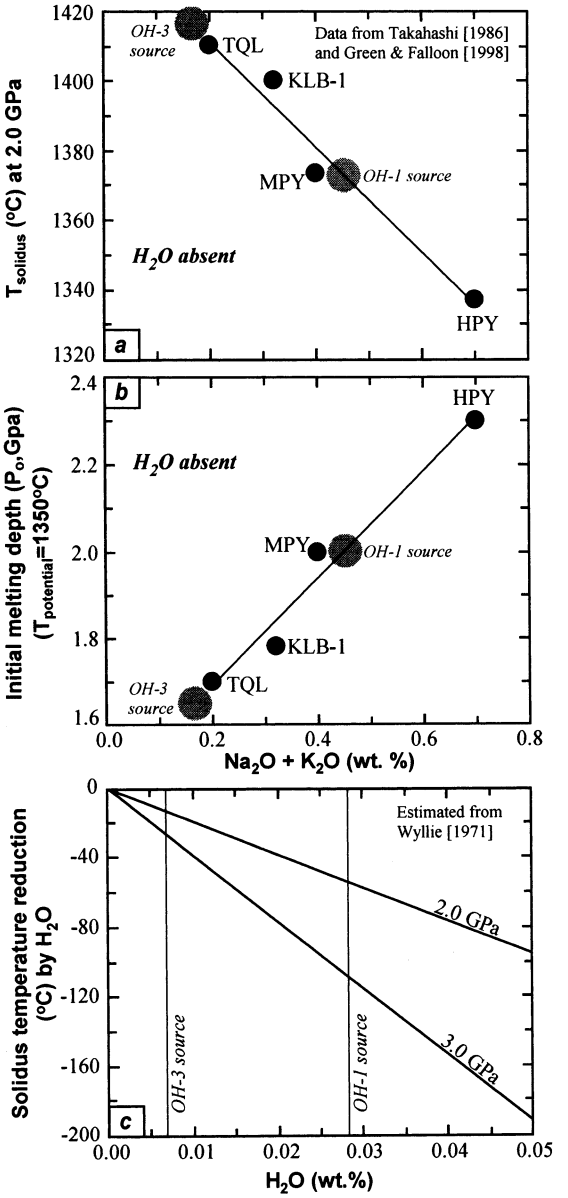

Fig. 6. a: Solidus temperature of anhydrous peridotites at a given pressure (e.g. 2 GPa) decreases with increasing total alkali (Na_2O+K_2O) contents. HPY, MPY and TQL are model mantle compositions studied experimentally by [59] and KLB-1 by [60]. The total alkali contents for a mean OH-1 source (~0.36 wt% Na_2O and ~0.09% K_2O) and a mean OH-3 source (<0.17% Na_2O and <0.01% K_2O) are estimated by using the average data, mean extents of melting calculated in Fig. 7, and polybaric melting models of Niu and Batiza [13,28]. b: This shows the fact that the depth at which an ascending mantle begins to melt varies significantly, depending on its fertility (total alkalis) even if the mantle potential temperature is assumed to be the same (e.g. 1350°C). c: The effect of H_2O in lowering the solidus temperature from a dry solidus is linearly interpolated from the solidus of wet peridotite with 0.1% H_2O by Wyllie [38]. Note that although experimental studies on hydrous peridotite melting exist (e.g. [38–41,59–62]), no constrained melting experiments on peridotites with <0.1% H_2O are available. Note also that the source water content for OH-1 (~280 ppm) and OH-3 (~70 ppm) is calculated as in Fig. 7.

explained by melting of compositionally distinct and heterogeneous mantle sources. That is, OH-1 lavas reflect a heterogeneous and enriched fertile source, whereas OH-3 lavas reflect a heterogeneous and depleted source. Regardless of detailed differences in fertile source mineralogy, mantle peridotites enriched in alkalis and other incompatible elements have lower solidus temperatures, thus begin to melt deeper, melt more, and produce more melts than peridotites depleted of these elements at a given mantle potential temperature as demonstrated in Fig. 6a,b. It is also well-established that H_2O, the most abundant volatile in Earth's mantle, behaves like an incompatible element (e.g. similar to K, La, Ce) during MORB genesis, and MORB melts enriched in incompatible elements always have elevated H_2O contents [36,37], reflecting their similar inheritance in the mantle sources. Therefore, OH-1 source (vs. OH-3 source) must also have elevated H_2O water contents, which further reduce the solidus temperature significantly (Fig. 6c). While further experimental refinement is needed, existing data indicate consistently that the effect of 0.05% (500 ppm) of H_2O in mantle peridotite is equivalent to lowering the solidus temperature in excess of 200°C at $\sim$100 km depth [38–41].

The actual water contents in the studied samples are unanalyzed, but it is straightforward to estimate water contents in these lavas using the observed H_2O–Ce relationship characteristic of North MAR MORB ($H_2O = 259.22 \times Ce + 172.14$; $r = 0.969$; in ppm) [37]. Calculations show that OH-1 lavas have 0.44 ± 0.24 wt% water whereas OH-3 lavas have on average only 0.19 ± 0.09 wt% water (see **EPSL Online Background Dataset**[1]). To determine precisely the amount of water present in the OH-1 and OH-3 mantle sources and its effect in enhancing the extent of melting is difficult, but the relative differences between OH-1 and OH-3 sources can be estimated satisfactorily as done for Ce in Fig. 7. Fig. 7a shows that the mean OH-1 source is significantly more enriched than the mean OH-3 source with more incompatible elements being more enriched than less incompatible ones as expected. For example, Nb in the OH-1 source is $\sim$20 times higher than in the OH-3 source, and Nd is only 2.5 times higher. Note the 4-fold H_2O enrichment in the OH-1 source relative to the OH-3 source. This difference in source H_2O abundances further promotes the greater extent of melting and melt production at OH-1 than at OH-3.

Fig. 7b plots primitive mantle normalized model elemental abundances in the OH-1 ($\sim$280 ppm H_2O) and OH-3 ($\sim$70 ppm) sources. The models also calculate that the average composition of OH-1 lavas can be produced by $F_{OH-1} = \sim 10\%$ melting of the OH-1 source, over twice as much as $F_{OH-3} = \sim 4.5\%$ melting for OH-3 lavas from the OH-3 source. The difference in the extent of melting between OH-1 and OH-3 must, however, be intrinsically related to their differences in source fertility (i.e. alkali and H_2O abundances etc.). Assuming a mantle potential temperature of 1350°C, then the depleted OH-3 mantle source with $\sim$70 ppm H_2O begins to melt at <2 GPa ($< \sim 60$ km), whereas the enriched OH-1 source with $\sim$280 ppm H_2O begins to melt at $\sim$3 GPa ($\sim$90 km) (Fig. 8). This difference in the initial depth of melting (P_o) is considerable and has important consequences. Clearly, the more fertile OH-1 mantle begins to melt deeper, has greater melting interval, and thus melts to a greater extent than the more refractory OH-3 mantle. It is also likely that the more fertile OH-1 mantle will produce more melt per unit pressure release than OH-3 mantle, thus contributing to the greater extent of melting of the OH-1 mantle. This also explains the 'garnet signature' conspicuous in OH-1 lavas but not so in OH-3 lavas (e.g. $Zr/Y_{OH-1} = 3.46 \pm 1.26 > Zr/Y_{OH-3} = 2.15 \pm 0.44$; $[Sm/Yb]_{N,OH-1} = 1.35 \pm 0.37 > [Sm/Yb]_{N,OH-3} = 1.02 \pm 0.12$).

Importantly, inefficient melt–solid separation at slow-spreading environment leads to significant melt-retention in the upwelling and melting mantle [42,43], which in turn promotes buoyant upwelling and enhances pressure release melting, crustal production, residual mantle depletion and density reduction – enhanced along-axis gravity low. This effect ultimately leads to focused 3-D upwelling on ridge segment scales [3,4,44]. Such melt-retention enhanced focused upwelling must be better developed beneath OH-1 than beneath OH-3 as no melt forms beneath the latter until the

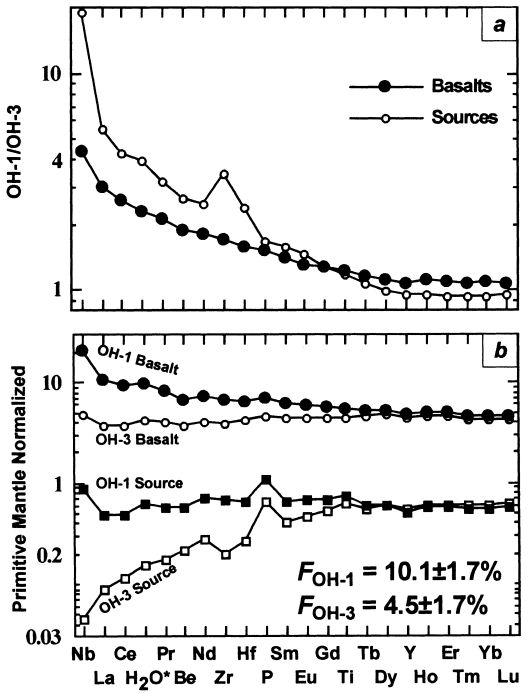

Fig. 7. a: Ratios of average OH-1 lava compositions over average OH-3 lava compositions plotted for trace elements in the order of decreasing incompatibility [32]. H_2O* is calculated H_2O content (see **EPSL Online Background Dataset**[1]). The estimated source ratios are plotted to show that the observed lava compositional differences between OH-1 and OH-3 are inherited from their respective sources. b: Primitive mantle [63] normalized trace elemental abundances of average OH-1 and OH-3 lavas and their respective model source abundances. The average OH-1 lavas can be produced by 10.1 ± 1.7% non-modal batch melting of the OH-1 source, whereas the average OH-3 lavas represent 4.5 ± 1.7% non-modal batch melting of the OH-3 source. The source ratios, source abundances, and the extents of melting are estimated as follows based on a number of assumptions. Assuming Ba, the most incompatible element among commonly analyzed trace elements [32], has a bulk distribution coefficient $D^{Ba} = 0$, we can plot C^{Ba}/C^i against C^{Ba} (C^{Ba} and C^i are contents of Ba and element i in lavas). This gives a linear equation of the form $C^{Ba}/C^i = S^i C^{Ba} + I^i$ (Equation 1) [64,65] for each element i considered for OH-1 and OH-3 sample suites respectively. The slopes, $S^i = D^i_o/C^i_o$ (Equation 2), and intercepts, $I^i = C^{Ba}_o/C^i_o(1-P^i)$ (Equation 3), are readily obtained by linear regressions, most of which have $r \geq 0.9$, statistically significant at $>99\%$ confidence levels. Where C^{Ba}_o and C^i_o are source abundances of Ba and element i; D^i_o is the initial bulk distribution coefficient of element i, and P^i is the effective bulk distribution coefficient of element i depending on mineral melting modes [64,65]. Assuming D^i_o is the same for both OH-1 and OH-3 (a reasonable approximation for this purpose, but not true for P^i), then the source ratio $C^{i,OH-1}_o/C^{i,OH-3}_o = S^{i,OH-3}/S^{i,OH-1}$ (Equation 4) as plotted in a. The source abundances for OH-3 are estimated from $C^i_o = D^i_o/S^i$ (Equation 5), where D^i_o is calculated by assuming melting in the spinel lherzolite stability field with initial modes of 55% olivine, 30% orthopyroxene, 13% clinopyroxene, and 2% spinel [66], and by using published mineral–basalt partition coefficients (see [66] for compilation). The extent of melting for OH-3 is calculated using $F = (C^{i,OH-3}_o/C^i - D^i_o)/(1-P^i)$ (Equation 6), where P^i is calculated using the same mineral–basal partition coefficient data and the decompression melting modes of [13]: 0.466 Cpx+0.681 Opx+0.048 Spl = 0.193 Ol+1 Melt. $F_{OH-3} = 4.5 \pm 1.7\%$ is the average and 1σ value of calculated F considering all the rare-earth elements in all the OH-3 samples with $[La/Sm]_N < 1$. The source abundances for OH-1 were calculated by combining Equations 3 and 4. Calculating the extent of melting for OH-1 is not straightforward because I^i values are negative for most heavy rare-earth elements, suggesting $P^i > 1$, and garnet must be a residual phase holding back heavy rare-earth elements. Thus, the polybaric decompression melting reaction for melting in the spinel lherzolite depth range does not apply. However, by assuming $C^{Ba}_o = 5.32$ ppm ($C^{Nb}_o \times 8.58$, a value assumed to be Ba/Nb ratio in the highly enriched sources), we then solved F and P^i simultaneously by iteration (combining Equations 3 and 6) by minimizing the relative standard deviation of average F values obtained by considering all the rare-earth elements. $F_{OH-1} = 10.1 \pm 1.7\%$ is such an average and 1σ value. These calculated values in the extent of melting should not be taken as definite, but they do argue persuasively that the observed differences in morphology, topography, crustal thickness and MBA between OH-1 and OH-3 result from different extents of melting and overall melt production ultimately controlled by fertile mantle source compositional differences. Note that the apparent Zr–Hf anomalies in the calculated sources or source ratios result form the published K_d values used, and may have no significance.
←

rising mantle reaches a much shallower level (Fig. 8b). This interpretation is consistent with all the observations (Figs. 1–7).

4.2. The relationship between MBA and magmatic segmentation at slow-spreading ridges

There is agreement that along-axis MBA variation within a ridge segment reflects crustal thickness variation – more negative MBA associated with thickened crust at segment center and weak MBA with thin crust at segment ends. That is, melt formed in the mantle is delivered more to the segment center than to the segment ends. It could be that such along-axis variations in melt

delivery result from along-axis variation in melt production. For example, the extent of melting may be high in the segment center and low near the offsets due to subdued upwelling or cold-edge effects [44,45]. It is also possible that there is substantial subcrustal melt migration and focusing towards segment center and the crustal thickness variation results from melt redistribution from the segment center to segment ends at the crustal level [7,17,45,46]. We can better understand melt delivery processes by analyzing current mantle flow models for the MAR.

There are two classes of models: focused mantle upwelling represented by Lin and co-authors [3,4] and 3-D melt migration by Madge and co-authors [7,46]. The former suggests that magmatic accretion along the MAR is characterized by focused mantle upwelling and melting at discrete centers initiated by a Rayleigh–Taylor gravitational instability developed in the partial melt zone [47–49]. Such focused upwelling develops because of melt-retention enhanced buoyancy with hotter and faster upwelling in the center and colder and retarded upwelling at the edges. As a result, more melt is produced by decompression in the segment center than near the edges, which explains, if melt migrates vertically, the thickened crust and more negative MBA in the segment centers. The 3-D melt migration model requires uniform mantle upwelling with varying final depth of melting limited by the 'cold' lithospheric lid that is thin in the segment centers and thickened beneath offsets. Melt migration is directed by the slopes of the lid towards the segment center, and delivered to the crust. Melt redistribution in the crust from the center to the segment ends is invoked to explain the observed along-axis crustal thickness variation. The fundamental difference between these two models is the cause–effect relationship between magmatism and ridge segmentation. In the focused mantle upwelling model, ridge segmentation is the consequence of focused upwelling at discrete centers. In the 3-D melt migration model however, pre-existing offsets determine melt migration.

We can test these two models against observations. Our preferred model is one that explains the significant inverse correlations of axial MBA variation with ridge segment length (Fig. 5), and the observation that enriched lavas prefer to occupy segment centers (Fig. 3). The test shows that the focused upwelling model is consistent with the observations although 3-D melt migration cannot be entirely ruled out. However, a unified model may emerge from these two models if the effect of fertile mantle compositional variation is considered (see Fig. 8).

4.2.1. The origin of the inverse correlation of MBA variation with segment length

The significant correlation of axial MBA variation with ridge segment length (Fig. 5a) points to a genetic link between the two parameters. The inverse correlation of ridge offset size (Fig. 5b) and the non-correlation of segment length/offset ratio with MBA variation (Fig. 5c) indicate that the ultimate process responsible for the MBA variation is deep and sublithospheric as it is unaffected by the 'cold-edge' effect at shallow levels. This observation is not in favor of 3-D melt migration model whose action is determined by the cold-edge and cold-lid effects at shallow mantle. 3-D melt migration may be invoked to qualitatively explain the inverse correlation between segment length and axial MBA variation as longer segments would produce more melt which, when largely focused at the segment centers, would lead to thicker crust and more negative MBA [24]. This action is, however, far inadequate to explain the inflated morphology, topography and thickened mean crust at long ridge segments like OH-1.

In contrast, the focused mantle welling model explains all these observations. For example, large buoyancy-driven mantle 'thermals' or 'diapirs' by their size upon development would lead to longer spreading segments because segmentation is determined by the discrete centers of focused mantle upwelling. Longer segments of wide zones of focused upwelling possess greater thermal gradients with hotter and faster ascent in the center, thus leading to a greater extent of decompression melting and more melt production beneath segment centers of longer segments than short segments. Therefore, longer segments (e.g. OH-1) are associated with thicker crust and more negative MBA

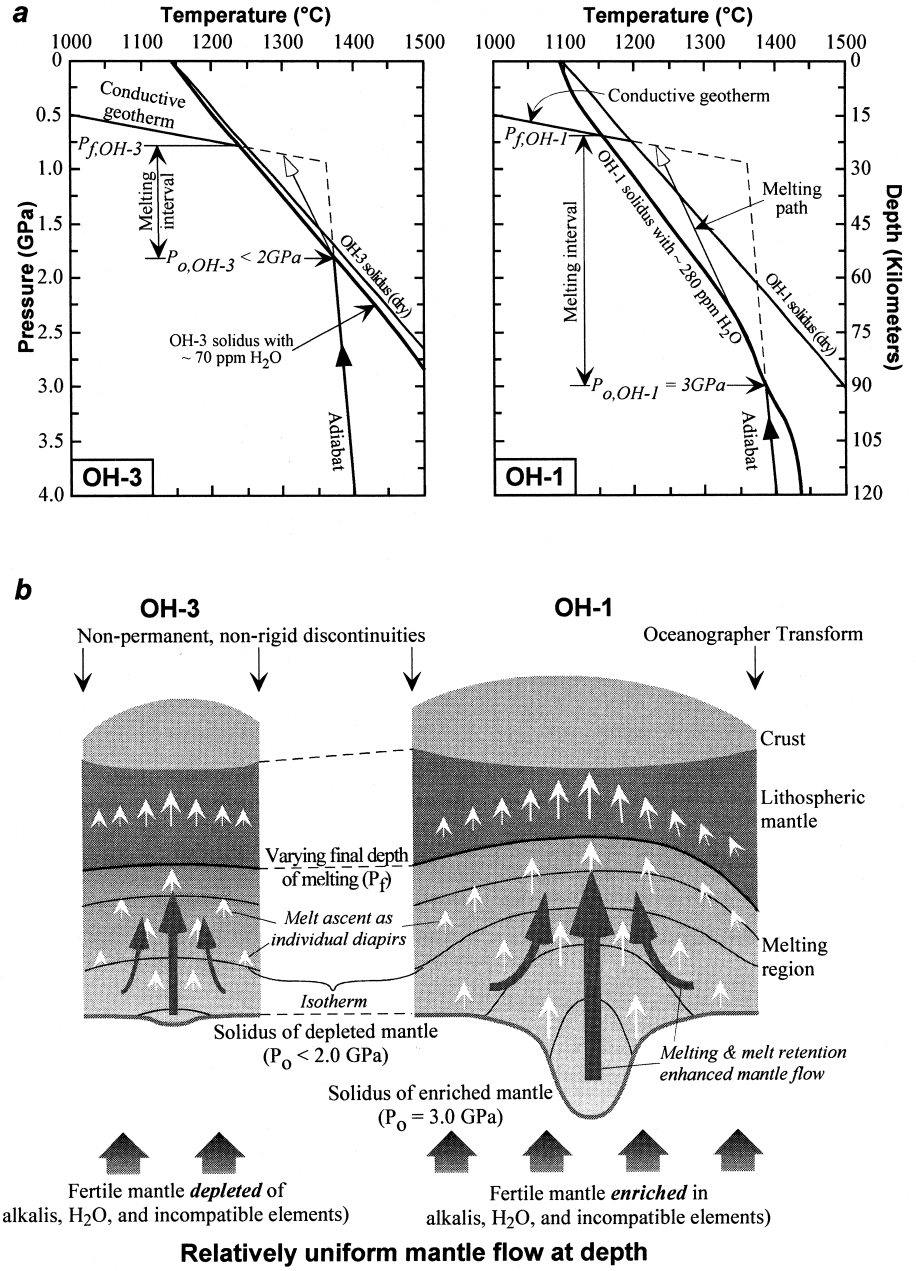

than short segments (e.g. OH-3). Focused flows are 3-D features, and their latitudinal growth or shrink may be accompanied by changes in their longitudinal dimension. Therefore, the offset size of a ridge segment may be genetically associated with such changes, thus leading to the inverse correlation between the offset size and axial MBA variation (Fig. 5b). Such a correlation, however, cannot be perfect because the measured offset size results from the growth/shrink of two adjacent ridge segments at probably different rates. A careful examination of the relationship between segment length and offset size as a function of time using the existing data [50,51] is

Fig. 8. a: Quantitative representation showing the differences in the initial depth of melting (P_o), melting depth range (P_o–P_f), thus the extent of melting and melt production between OH-1 and OH-3 because of fertile source compositional differences (alkalis, H_2O and other incompatible elements) even if the mantle potential temperature is the same (e.g. 1350°C). Assuming a mantle potential temperature of 1350°C, the depleted OH-3 mantle begins to melt at depth <2 GPa, but the enriched OH-1 mantle would begin to melt at a significantly greater depth, probably ~ 3 GPa Kb. Consequently, OH-1 mantle will have a taller melting interval and melt more than OH-3 mantle. The dry solidi are modified from [67] considering the data in Fig. 6a,b. The wet solidi are linearly interpolated from the solidus of wet peridotite with 0.1% H_2O by [38]. b: Cartoons showing along-axis differences between OH-1 and OH-3 in the mantle region of upwelling, melting and melt extraction. While mantle upwelling may be uniform at great depth, focused upwelling begins to develop upon melting because of melt-retention and residue density reduction induced buoyancy. Such buoyancy-driven flow, which ascends at elevated rates with enhanced decompression melting and melt production, is clearly better developed in the OH-1 mantle, not in the OH-3 mantle where no melt forms until the ascending mantle reaches a shallower level. In this model, decompression melting and melt production are highest in the center and decline towards the offsets because of the enhanced upwelling rate in the center. Also, we suggest melt migration and delivery to the crust take vertical paths via small 'diapirs' (white arrows) as proposed by [44] without significant subcrustal melt migration and focusing. Thus, the observed along-axis crustal thickness variation reflects along-axis melt production. This model also explains why enriched or less depleted lavas prefer to occupy the segment centers (see text for details).
←

needed to quantify the significance of the correlation in Fig. 5b. We emphasize in this context that, as we know, non-transform discontinuities are not permanent offsets, but can migrate as a result of the growth of one ridge segment at the expense of its neighboring segments [33,52,53]. Therefore, it is sublithospheric, not lithospheric, mantle processes that determine the nature and history of a non-permanent discontinuity, not the opposite even though these discontinuities may affect melt migration/distribution in the crust if any.

4.2.2. *Why geochemically enriched lavas prefer to occupy the center of a segment?*

Fig. 3 shows that while depleted lavas occur along the entire length of a ridge segment, enriched (OH-1) or less depleted (OH-3) lavas within a segment preferentially occur at the segment center. This phenomenon is also observed at some ridges in the Pacific [54,55], and in particular at many well-sampled MAR segments [17,33,45], thus is probably a general consequence of magmatic accretion at the MAR. This observation can be explained by the model of focused mantle upwelling (Fig. 8b). According to this model, the erupted lavas are delivered vertically from the mantle by individual 'diapirs' (white arrows). Thus, the along-axis lava geochemical variation reflects such a variation in the primary mantle melts. The enriched lavas at the segment center require enriched fertile mantle beneath the center. The thickened crust at the segment center requires high extents of melting and great melt production beneath the center. Both these requirements are consistent with discrete distributions of enriched mantle heterogeneities that trigger Rayleigh–Taylor type instabilities or 'thermals' when they ascend to their solidus depths. The size and fertility (i.e. the effect of alkali and H_2O contents as in Fig. 6) of the enriched heterogeneities determine the initial depth of melting and the size/length of the focused upwelling system. A large, and long-lived enriched domain (regardless of its ultimate origin and history) in the OH-1 mantle has resulted in a large focused upwelling system whereas a probably very small amount of enriched material in the OH-3 mantle led only to a small and weak focused upwelling system (Fig. 8b). Hence, the preferred occurrence of enriched or less depleted lavas at segment centers is a consequence of the processes we propose in Fig. 8.

The 3-D melt migration model, however, cannot explain why enriched lavas prefer to occur at segment center. Subcrustal focusing of melts produced along the entire segment length towards segment center would effectively homogeneize these melts before and during delivery to the crust. As a result, the erupted melts within a ridge segment would be compositionally uniform, but this is not the case. Furthermore, melt redistribution from segment center towards offsets in the crust would lead to systematic decrease in lava eruption temperature (e.g. MgO) as seen in many segments along the EPR [56,57], but this

is not observed either. Enriched melts with high H_2O contents have lower solidus temperatures. These melts thus have the potential to travel a greater distance towards the offsets before solidification. Consequently, enriched melts would be expected to occur near offsets, not at segment centers, which is again not observed. In fact, lavas from many MAR segments are compositionally diverse and require individual mantle melt batches directly delivered to the crust with their own cooling histories [33,44,45].

Alternatively, great melt production and delivery at segment centers may allow the development of magma chambers at segment centers, which, through 'periodic replenishment, periodic eruption, and advanced and continuous fractionation' [58], may contribute to the enrichments in lavas erupted at segment centers. This process is certainly important, if a steady-state magma chamber is developed, and can explain the elevated abundances of incompatible elements, but is inadequate to explain elevated ratios of incompatible elements (e.g. $[La/Sm]_N$, $[Sm/Yb]_N$, Nb/Zr, Zr/Y) in lavas erupted at the center of OH-1 without invoking (1) an unusually enriched fertile mantle source, and (2) deep initial melting evidenced by the 'garnet signatures' (e.g. high $[Sm/Yb]_N$).

4.2.3. *Suggestion for a unified model for magmatic accretion at the MAR*

While focused mantle upwelling model [3,4] with vertical melt delivery to the crust [44] better explains both geophysical and geochemical observations than subcrustal melt migration model [7,46], the current focused upwelling model cannot explain why some upwelling systems are developed larger (longer ridge segments) than others given the more or less uniform mantle potential temperature in a geographically small area such as the Oceanographer–Hayes region. It is perhaps this drawback that led to the rejection of the focused upwelling model because indeed the model results [7,46] demonstrate that buoyant flows have along-axis wavelengths greater than 150 km, and thus cannot produce the observed size of ridge segments, which are variably shorter (e.g. 10–100 km). We expect future mantle flow models that consider the effect of fertile mantle compositional variation (see Figs. 6–8) to succeed in producing along-axis wavelengths of buoyant flows comparable to the observed size of ridge segmentation at the MAR.

5. Summary

1. The contrasting differences in morphology, topography, crustal mass, and MBA between OH-1 and OH-3 result from fertile mantle compositional difference beneath the two ridge segments.
2. Focused mantle upwelling and melting with vertical melt delivery to the crust best explains both geophysical and geochemical observations at the MAR.
3. The size of focused upwelling is controlled by the size and fertility of the enriched domains passively embedded in the sub-ridge mantle. The size and fertility of the enriched domains may actually control the initiation and evolution of ridge segments bounded by non-rigid discontinuities at slow-spreading ridges.
4. Mantle source compositional variation, as are mantle temperature variation and plate spreading rate variation, is a fundamental variable that determines the physical behavior of the upwelling and melting mantle as well as the extent of mantle melting, crustal production and MORB chemistry.

Acknowledgements

We thank the captain and crew of the R/V *Nadir* and the *Nautile* group for making the sampling program successful. Y.N. acknowledges support from The University of Queensland and ARC. D.B. and R.H. thank for support from IFREMER and French Ministere des Affairs Etrangeres. R.B. thanks for support from the University of Hawaii and NSF. Discussion with Allegra Hosford and Jian Lin was helpful. Formal reviews by Wolfgang Bach and an unnamed reviewer are acknowledged.***[FA]***

References

[1] K.C. Macdonald, Mid-ocean ridges: Fine scale tectonic, volcanic, and hydrothermal processes within the plate boundary zone, Ann. Rev. Earth Planet. Sci. 10 (1982) 155–190.

[2] J.-C. Sempéré, G.M. Purdy, H. Schouten, Segmentation of the Mid-Atlantic Ridge between 24°N and 34°N40′N, Nature 344 (1990) 427–431.

[3] J. Lin, G.M. Purdy, H. Schouten, J.-C. Sempéré, C. Zervas, Evidence from gravity data for focused magmatic accretion along the Mid-Atlantic Ridge, Nature 344 (1990) 627–632.

[4] J. Lin, J. Phipps Morgan, The spreading rate dependence of three-dimensional mid-ocean ridge gravity structure, Geophys. Res. Lett. 19 (1992) 13–16.

[5] R.S. Detrick, H.D. Needham, V. Renard, Gravity anomalies and crustal thickness variations along the Mid-Atlantic Ridge between 33°N and 40°N, J. Geophys. Res. 100 (1995) 3767–3787.

[6] M. Tolstoy, A.J. Harding, J.A. Orcutt, Crustal thickness on the Mid-Atlantic Ridge: Bull's eye gravity anomalies and focused accretion, Science 262 (1993) 726–729.

[7] L.S. Magde, D.W. Sparks, R.S. Detrick, The relationship between buoyant mantle flow, melt migration, and gravity bull's eyes at the Mid-Atlantic Ridge between 33°N and 35°N, Earth Planet. Sci. Lett. 148 (1997) 59–68.

[8] R.S. Detrick, J. Collins, G. Kent, J. Lin, D. Toomey, A. Barclay, E. Hooft, A. Hosford, S. Hussenoeder, Mid-Atlantic Ridge bull's-eye experiment: A seismic investigation of segment-scale crustal heterogeneity at a slow-spreading ridge, InterRidge News 6 (1997) 27–32.

[9] J.N. Natland, Partial melting of a lithologically heterogeneous mantle: Inferences from crystallization histories of magnesian abyssal tholeiites from the Siqueiros Fracture Zone, in: A.D. Saunders, M.J. Norry (Eds.), Magmatism in the Ocean Basins, Geological Society Special Publication, 42, 1989, pp. 41–70.

[10] F. Albarède, How deep do common basaltic magmas form and differentiate? J. Geophys. Res. 97 (1992) 10997–11009.

[11] Y. Shen, D.W. Forsyth, Geochemical constraints on initial and final depth of melting beneath mid-ocean ridges, J. Geophys. Res. 100 (1995) 2211–2237.

[12] Y. Niu, K.D. Collerson, R. Batiza, I. Wendt, M. Regelous, The origin of E-type MORB at ridges far from mantle plumes: The East Pacific Rise at 11°20′N, J. Geophys. Res. 104 (1999) 7067–7087.

[13] Y. Niu, Mantle melting and melt extraction processes beneath ocean ridges: Evidence from abyssal peridotites, J. Petrol. 38 (1997) 1047–1074.

[14] J.-G. Schilling, Azores mantle blob: Rare earth evidence, Earth Planet. Sci. Lett. 25 (1975) 103–115.

[15] J.-G. Schilling, M. Zajac, R. Evans, T. Johnston, W. White, J.D. Devine, R. Kingsley, Petrological and geochemical variations along the Mid-Atlantic Ridge from 29°N to 73°N, Am. J. Sci. 283 (1983) 510–586.

[16] H.D. Needham, SIGMA Scientific Team, The crest of the Mid-Atlantic Ridge between 40° and 15°N: Very broad swath mapping with the EM 12 echo sounding system, EOS 72 (1991) 470.

[17] C.H. Langmuir, J. Reynolds, H. Bougault, T. Plank, L. Dosso, D. Desonie, E. Gier, Y. Niu, A petrological traverse along the Mid-Atlantic Ridge across the Azores hotspot, J. Conf. Abstr. 1 (1996) 834–835.

[18] L. Dosso, H. Bougault, C. Langmuir, C. Bollinger, O. Bonnier, J. Etoubleau, The age and distribution of mantle heterogeneity along the Mid-Atlantic Ridge (31–41°N), Earth Planet. Sci. Lett. 170 (1999) 269–286.

[19] D. Bideau, R. Hékinian, C. Bollinger, M. Constantin, E. Grácia, C. Guivel, B. Sichler, R. Appriroual, R. Le Gall, Submersible investigation of highly contrasted magmatic activities recorded on two segments of the Mid-Atlantic Ridge near 34°52′N and 33°55′N, InterRidge News 5 (1996) 9–14.

[20] D. Bideau, R. Hékinian, B. Sichler, E. Gràcia, C. Bollinger, M. Constantin, C. Guivel, Contrasting volcanic–tectonic processes during the past 2 Ma on the Mid-Atlantic Ridge: submersible mapping, petrological and magnetic results at lat. 34°52′N and 33°55′N, Mar. Geophys. Res. 20 (1998) 425–458.

[21] E. Gràcia, D. Bideau, R. Hékinian, Y. Lagabrielle, L.M. Parson, Along-axis magmatic oscillations and exposure of ultramafic rocks in a second-order segment of the mid-Atlantic ridge (33°43′N–34°07′N), Geology 25 (1997) 1059–1062.

[22] E. Gràcia, D. Bideau, R. Hékinian, Y. Lagabrielle, Detailed mapping of two contrasting second-order segments of the mid-Atlantic ridge between Oceanographer and Hayes fractures zones (33°30′N–35°N), J. Geophys. Res. 104 (1999) 22903–22921.

[23] A.H. Barcalay, D.R. Tommey, S.C. Solomon, Seismic structure and crustal magmatism at the Mid-Atlantic Ridge, 35°N, J. Geophys. Res. 103 (1998) 17827–17844.

[24] E.E.E. Hooft, R.S. Detrick, D.R. Toomey, J.A. Collins, J. Lin, Crustal thickness and structure along three contrasting spreading segments of the Mid-Atlantic Ridge, 33.5°–35°N, J. Geophys. Res. 105 (2000) 8205–8226.

[25] A. Hosford, J. Lin, R.S. Detrick, Crustal evolution over the last 2 Ma at the Mid-Atlantic Ridge OH-1 segment, 35°N, J. Geophys. Res. (in press).

[26] R. Hékinian, F. Pineau, S. Shilobreeva, D. Bideau, E. Gràcia, M. Jovoy, Deep seated explosive activity on the Mid-Atlantic Ridge near 34°50′N: Magma composition, vascularity and volatile content, J. Volcan. Geotherm. Res. (in press).

[27] E.M. Klein, C.H. Langmuir, Global correlations of ocean ridge basalt chemistry with axial depth and crustal thickness, J. Geophys. Res. 92 (1987) 8089–8115.

[28] Y. Niu, R. Batiza, An empirical method for calculating melt compositions produced beneath mid-ocean ridges: application for axis and off-axis (seamounts) melting, J. Geophys. Res. 96 (1991) 21753–21777.

[29] C.H. Langmuir, E.M. Klein, T. Plank, Petrological sys-

tematics of mid-ocean ridge basalts: Constraints on melt generation beneath ocean ridges, in: J.P. Morgan, D.K. Blackman, J.M. Sinton (Eds.), Mantle Flow and Melt Generation at Mid-Ocean Ridges, AGU Monograph., 71, 1992, pp. 183–280.

[30] Y. Niu, R. Hékinian, Spreading rate dependence of the extent of mantle melting beneath ocean ridges, Nature 385 (1997) 326–329.

[31] J. Cotton, A. Le Dez, M. Bau, M. Caroff, R.C. Maury, P. Dulski, S. Fourcade, M. Bohn, R. Brousse, Origin of anomalous rare-earth elements and yttrium enrichments in subaerially exposed basalts: Evidence from French Polynesia, Chem. Geol. 119 (1995) 115–138.

[32] Y. Niu, R. Batiza, Trace element evidence from seamounts for recycled oceanic crust in the eastern equatorial Pacific mantle, Earth Planet. Sci. Lett. 148 (1997) 471–484.

[33] P.J. Michael et al., Mantle control of a dynamically evolving spreading center, Earth Planet. Sci. Lett. 121 (1994) 451–468.

[34] D.W. Forsyth, Geophysical constraints on mantle flow and melt generation beneath mid-ocean ridges, in: J.P. Morgan, D.K. Blackman, J.M. Sinton (Eds.), Mantle Flow and Melt Generation at Mid-Ocean Ridges, AGU Monograph., 71, 1992, pp. 1–66.

[35] C. DeMets, R.G. Gordon, D.F. Argus, S. Stein, Current plate motions, Geophys. J. Int. 101 (1990) 425–478.

[36] K.E.D. Aggrey, D.W. Muenow, R. Batiza, Volatile abundances in basaltic glasses from seamounts flanking the East Pacific Rise at 21°–14°N, Geochim. Cosmochim. Acta 52 (1988) 2115–2119.

[37] P.J. Michael, Regionally distinctive sources of depleted MORB: Evidence from trace elements and H_2O, Earth Planet. Sci. Lett. 131 (1995) 301–320.

[38] P.J. Wyllie, Role of water in magma generation and initiation of diapiric uprise in the mantle, J. Geophys. Res. 76 (1971) 1328–1338.

[39] D.H. Green, Experimental melting studies on a model upper mantle composition at high pressure under water-saturated and under-saturated conditions, Earth Planet. Sci. Lett. 19 (1973) 37–53.

[40] B.O. Mysen, A.L. Boettcher, Melting of a hydrous mantle: II. Geochemistry of crystals and liquids formed by anatexis of mantle peridotite at high pressures and high temperatures as a function of controlled activities of water, hydrogen, and carbon dioxide, J. Petrol. 16 (1975) 549–593.

[41] E. Stolper, S. Newman, The role of water in the petrogenesis of Mariana trough magmas, Earth Planet. Sci. Lett. 121 (1994) 293–325.

[42] D.R. Scott, D.J. Stevenson, A self-consistent model of melting, magma migration and buoyancy-driven circulation beneath mid-ocean ridges, J. Geophys. Res. 94 (1989) 2973–2988.

[43] C. Sotin, E.M. Parmentier, Dynamic consequences of compositional and thermal density stratification beneath spreading centers, Geeophys. Res. Lett. 16 (1989) 835–838.

[44] Y. Niu, R. Batiza, Magmatic processes at the Mid-Atlantic ridge ~26°S, J. Geophys. Res. 99 (1994) 19719–19740.

[45] J.R. Reynolds, C.H. Langmuir, Petrological systematics of the mid-Atlantic ridge south of Kane: Implications for ocean crust formation, J. Geophys. Res. 102 (1997) 14915–14946.

[46] L.S. Magde, D.W. Sparks, Three-dimensional mantle upwelling, melt generation, and migration beneath segmented slow-spreading ridges, J. Geophys. Res. 102 (1997) 20571–20583.

[47] J.A. Whitehead, H.J.B. Dick, H. Schouten, A mechanism for magmatic accretion under spreading centers, Nature 312 (1984) 146–147.

[48] H. Schouten, K.D. Klitgord, J.A. Whitehead, Segmentation of mid-ocean ridges, Nature 317 (1985) 225–229.

[49] K. Crane, The spacing of rift axis highs: Dependence on diapiric processes in the underlying asthenosphere, Earth Planet. Sci. Lett. 72 (1985) 405–415.

[50] J. Lin, B.E. Tucholke, M.C. Kleinrock, Off-axis crustal structure of the Mid-Atlantic Ridge, InterRidge News 6 (1997) 23–26.

[51] B.E. Tucholke, J. Lin, M.C. Kleinrock, M.A. Tivey, T.B. Reed, J. Goff, G. Jaroslow, Segmentation and crustal structure of the western mid-Atlantic ridge flank, 25°30′–27°10′N and 0–29 Ma, J. Geophys. Res. 102 (1997) 10203–10223.

[52] N.R. Grindlay, P.J. Fox, K.C. Macdonald, Second order ridge axis discontinuities in the South Atlantic: Morphology, structure, and evolution, Mar. Geophys. Res. 13 (1991) 21–49.

[53] P. Gente, R.A. Pockalny, C. Durand, C. Deplus, M. Maia, G. Ceuleneer, C. Mével, M. Cannat, C. Lavarne, Characteristics and evolution of the Mid-Atlantic Ridge between 20°N and 24°N during the last 10 million years, Earth Planet. Sci. Lett. 129 (1995) 55–71.

[54] J.L. Karsten, J.R. Delaney, J.M. Rhodes, R.A. Lilias, Spatial and temporal evolution of magmatic systems beneath the Endeavor segment Juan de Fuca ridge: Tectonic and petrologic constraints, J. Geophys. Res. 95 (1990) 19235–19256.

[55] M.R. Perfit, D.J. Fornari, Geochemical studies of abyssal lavas recovered by DSRV Alvin from eastern Galapagos Rift, Inca Transform, and Ecuador Rift: 2, Phase chemistry and crystallization history, J. Geophys. Res. 88 (1983) 10530–10550.

[56] R. Batiza, Y. Niu, Petrology and magma chamber processes at the East Pacific Ridge ~9°30′N, J. Geophys. Res. 97 (1992) 6779–6797.

[57] M. Regelous, Y. Niu, J.I. Wendt, R. Batiza, A. Greig, K.D. Collerson, An 800 ka record of the geochemistry of magmatism on the East Pacific Rise at 10°30′N: Insights into magma chamber processes beneath a fast-spreading ocean ridge, Earth Planet. Sci. Lett. 168 (1999) 45–63.

[58] M.J. O'Hara, R.E. Mathews, Geochemical evolution in an advancing, periodically replenished, periodically tapped, continuously fractionated magma chamber, J. Geol. Soc. Lond. 138 (1981) 237–277.
[59] D.H. Green, T.J. Falloon, Pyrolite: A Ringwood concept and its current expression, in: I. Jackson (Ed.), The Earth's Mantle, composition, Structure, and Evolution, Cambridge University Press, 1998, pp. 311–380.
[60] E. Takahashi, Melting of a dry peridotite KLB-1 up to 14 GPa: Implications on the origin of peridotitic upper mantle, J. Geophys. Res. 91 (1986) 9367–9382.
[61] G.A. Gaetani, T.L. Grove, The influence of water on melting of mantle peridotite, Contrib. Mineral. Petrol. 131 (1998) 323–346.
[62] K. Hirose, Melting experiments on lherzolite KLB-1 under hydrous conditions and generation of high-magnesian andesitic melts, Geology 25 (1997) 42–44.
[63] S.-s. Sun, W.F. McDonough, Chemical and isotopic systematics of ocean basalt: Implications for mantle composition and processes, in: A.D. Saunders, M.J. Norry (Eds.), Magmatism of the Ocean Basins, Geol. Soc. Lond. Spec. Publ. 42, 1989, pp. 323–345.
[64] D.M. Shaw, Trace element fractionation during anatexis, Geochim. Cosmochim. Acta 34 (1970) 237–243.
[65] A.W. Hofmann, M.D. Feigenson, Case studies on the origin of basalt: I. Theory and reassessment of Grenada basalts, Contrib. Mineral. Petrol. 84 (1983) 382–389.
[66] Y. Niu, R. Hékinian, Basaltic liquids and harzburgitic residues in the Garrett Transform: A case study at fast-spreading ridges, Earth Planet. Sci. Lett. 146 (1997) 243–258.
[67] D. McKenzie, M.J. Bickle, The volume and composition of melt generation by extension of the lithosphere, J. Petrol. 29 (1988) 625–679.